00421)
LEP/BI/cp

LEP Note 492
20th March, 1984

A BEAM PROFILE MONITOR USING SYNCHROTRON LIGHT

J. Kishiro*) and C. Bovet

1. INTRODUCTION

We study the feasibility of a vertical beam profile monitor for LEP which would detect synchrotron radiation (SR) without imaging, following an idea recently developped at PEP. Most methods proposed so far[1] have complicated optical systems in order to obtain a precise image in the detector plane. However, those equipments are difficult to align and to maintain. Furthermore, any imaging system suffers from aberrations, is diffraction limited, and must be designed with great care[2].

The principle of this measurement is based on the fact that the synchrotron radiation is strongly concentrated in a narrow cone, especially for small wave lengths. Thus the phase plane distribution of SR is not much different from that of electrons and the electron beam size can be inferred from a measurement of the photon profile.

In order to realize this aim SR detection could be achieved with silicon microstrips located near a defocusing quadrupole magnet where the electron beam does not use the full aperture of the standard vacuum chamber. Figure 1 shows the layout of the detector which observes SR emitted, 7 m downstream of the quadrupole magnet Q13. In front of the detector one radiation length of tungsten can be used to filter out the lower energy component of SR which otherwise would reduce the accuracy of the profile measurement because of its wider angular distribution.

---

*) on leave from Nat. Lab. for High Energy Physics (KEK), Ibaraki, Japan

2. SYNCHROTRON LIGHT

The electron beam generates photons in the tangential direction of motion and their intensity can be described by the following formula[3] :

$$\frac{d^2N}{d\varepsilon\, dt}\ \frac{\text{photons}}{\text{keV s}} = 1.50 \times 10^{17}\ \frac{g(r)}{r}\ \frac{I\,R}{E^2}\ \frac{mA\ m}{GeV^2} \qquad (1)$$

where g(r) is a function of the photon energy ($r = \varepsilon/\varepsilon_c$). E, I and R are the electron energy, electron current and average machine radius, respectively, ε_c is the critical energy of SR defined by[3] :

$$\varepsilon_c[\text{keV}] = 2.218\ \frac{E^3}{\rho}\ \frac{GeV^3}{m}\ . \qquad (2)$$

By substituting the parameters of LEP-13 the critical energy is 94.9 keV. Figure 2 shows the photon intensity versus energy.

The photon phase plane distribution will be obtained with a convolution of electron divergence and SR emission angle. Figure 3 shows the angular distribution, U(r,α), of SR in the vertical plane (perpendicular to the bending plane)[4], whereby the vertical angle ψ scales with r and γ as :

$$\psi = \alpha\, r^{-1/3}\, \gamma^{-1}. \qquad (3)$$

For $r \approx 1$ the distribution is nearly Gaussian with an r.m.s. value given by :

$$\psi_{r.m.s.} = \alpha_{r.m.s.}\ r^{-1/3}\, \gamma^{-1}\ . \qquad (4)$$

At the energy of LEP phase I, the Lorentz factor $\gamma \approx 10^5$ so that $\psi_{r.m.s.} \approx 6$ μrad at ε_c. As shown in Fig. 3 and by Equ. 4 the divergence $\psi_{r.m.s.}$ is wider for lower photon energy, (lower r). Thus we have interest to restrict the spectrum to high energies as much as possible in order to reduce the smearing out of the beam image by the angular spread of SR.

3. PHASE SPACE DISTRIBUTION

In general, the phase plane distribution of the electrons can be described by a Gaussian function :

$$f \sim e^{-\xi^2/2\sigma^2} \tag{5}$$

where $$\xi^2 = \gamma y^2 + 2\alpha yy' + \beta y'^2 \ .^{[5]} \tag{6}$$

When $\xi^2 = \varepsilon_v$ vertical emittance/π) then Equ. 6 describes an ellipse at one standard deviation. Let us transform the phase plane (y_a, y'_a) into (y_b, y'_b), in order to get an upright ellipse (see Fig. 4). This fictitious transformation is not altering the distribution versus y and for any given value of y it just shifts the distribution in y' by a constant value so that the first moment $\bar{y}'$vanishes, but the second moment remains unchanged.

$$\begin{pmatrix} y_b \\ y'_b \end{pmatrix} = M \begin{pmatrix} y_a \\ y'_a \end{pmatrix} \ , \quad M = \begin{pmatrix} 1 & 0 \\ \alpha_a/\beta_a & 1 \end{pmatrix} \tag{7}$$

By this transformation the Twiss parameters are also changed to :

$$\begin{aligned} \alpha_b &= 0 \\ \beta_b &= \beta_a \\ \gamma_b &= \gamma_a - \alpha_a^2/\beta_a \\ \beta_b\gamma_b &= 1 \end{aligned} \tag{8}$$

The new phase plane distribution can be written with separate variables :

$$f \sim e^{-y_b^2/2\sigma_y^2} \cdot e^{-y_b'^2/2\sigma_y'^2} \tag{9}$$

where $$\sigma_y = \sqrt{\varepsilon_v\beta_b} \quad \text{and} \quad \sigma_{y'} = \sqrt{\varepsilon_v\gamma_b} \ . \tag{10}$$

We now can easily combine the electron distribution with SR angles to get the photon divergence as :

$$\tilde{\sigma}_{y'}^2 = \sigma_{y'}^2 + \psi_{r.m.s.}^2 \tag{11}$$

According to equations (10) and (11), the Twiss parameters of the photon distribution become :

$$\begin{aligned} \tilde{\alpha} &= 0 \\ \tilde{\beta}/\tilde{\gamma} &= (\sigma_y/\tilde{\sigma}_{y'})^2 \\ \tilde{\beta}\tilde{\gamma} &= 1 \end{aligned} \qquad (12)$$

And the emittance is increased as :

$$\tilde{\varepsilon}_v = \frac{\tilde{\sigma}_{y'}}{\sigma_{y'}} \varepsilon_v \qquad (13)$$

Let us come back to the real phase space distribution of X-rays by applying the inverse transformation M^{-1} to the Twiss parameters $\tilde{\alpha}$, $\tilde{\beta}$ and $\tilde{\gamma}$. Figure 5 shows the resulting phase plane ellipse for X-rays and compares it to the original electron distribution. The beam profiles which should be observed by the detector can be obtained by transforming the above ellipses through the drift space between emission point and detector.

With LEP-13 parameters we get :

at emission point,

	for electrons	for X-rays
α	= -1.045	-0.853
β	= 35.682 m	29.150
γ	= 0.0587 m^{-1}	0.0593
ε_v	= 2400 • 10^{-12} rad m	2993 • 10^{-12}

at detector position,

	for electrons	for X-rays
α	= -2.077	-1.896
β	= 90.583 m	77.507
γ	= 0.0587 m^{-1}	0.0593
σ_y	= 466.2 µm	481.6

Note that the X-ray beam size is very close to the electron beam size (only 3.3 % difference) so that one can easily deduce the latter from measuring the former.

4. FIELD DEPTH

Ideally, we should observe SR emitted from a single point on the electron orbit. However, in the configuration described in the previous section, with an horizontal aperture of 10 mm the detector receives SR emitted through the following length on the orbit :

$$16.70 \text{ m} < L < 18.47 \text{ m},$$

where L is the distance measured from the lattice magnet Q12 (Fig. 6). A computation of X-ray beam size can be repeated, following the procedure of Section 3, for these two extreme positions of the SR source. The result shows a variation of the measured beam size of only 0.7 % thus the effect of field depth can be neglected.

5. FILTER

In the evaluation of Para. 3 we assumed that all photons have about the critical energy but in practice many more photons will be radiated at much lower energies. In order to avoid the smearing effect of the angular distribution of SR, the spectrum should be restricted by a high pass filter. This can be achieved with the insertion of an absorber in front of the detector.

Below 1 MeV photons interact with matter in two ways :

1) Photoelectric interaction,
2) Scattering :
   - Compton scattering,
   - Rayleigh scattering.

1) In the photoelectric effect the photon interacts with an atomic electron and looses its total energy. The cross-section of this effect can be written as[6,7] :

$$\sigma_{ph} \propto Z^{\alpha} \varepsilon^{-3} \qquad (14)$$

where Z and is the atomic number of the material and ϵ is the photon energy. Values for α range from 4 to 5. This effect can be used to create a high pass filter as suggested in Fig. 9.

2) The two scattering processes cause an energy degradation of the incident photons and spoils completely their angular distribution which is detremental to the accuracy of the profile measurement. Thus, we have to chose for the filter a material which has a large ratio, σ_{ph}/σ_{sc}, of cross-sections for photoelectric interaction and Compton plus Rayleigh scattering, repectively. Figure 7 illustrates these ratios for various materials.

For Tungsten the K-shell edge in its photoelectric cross-section falls inside the energy band of interest here so that the cross-section ratio has an abrupt jump near the photon energy of 70 keV. We chose to use a filter made of a 4 mm thick tungsten plate, because of its large cross-section ratio and of its steep energy dependence which causes a strong attenuation of low energy photons. Relevant cross-sections for tungsten and total absorption length λ_t are shown in Fig. 8. The resulting photon intensity at- tenuation factor is :

$$e^{-x/\lambda_t} , \qquad (15)$$

where $1/\lambda_t = n\rho/A\ (\sigma_{ph} + \sigma_{sc})$, and N, ρ and A are Avogadro's number, density and atomic number, respectively. This factor is il- lustrated in Fig. 9, for various thicknesses x . The energy degrada- tion and the widening of the divergence for photons traversing the tungsten plate are investigated by means of a computer simulation programme. The details of the programme are described in Section 7.

6. DETECTOR

A silicon microstrip detector could be particularly well suited to observe the X-ray profile.

A silicon detector works somewhat like an ionization chamber. The silicon slab has a p-layer, on one side, a n-layer on the other side and the voltage gradient develops a depletion layer inbetween. When an X-ray irradiates the detector electrons and positive holes are created in the p,n and depletion layer. These electrons and holes in the depletion layer diffuse into p and n layers, respectively, and the movement of those charges induces the output current signal.

Whether a photon is detected or not depends on its probability of being absorbed by photoelectric effect during its traversal of the silicon slab. This detection efficiency is shown on Fig. 10. Charged pairs are then created in proportion of the available energy divided by the pair creation energy, ϵ_{pair}, (3.8 eV for silicon)[8].

In terms of mobility, the transit time of charged pairs in the depletion layer is :

$$\tau_t = \frac{d}{v_{drift}} = \frac{d^2}{\mu U} \qquad (16)$$

where μ, U and d are the mobility, the applied bias voltage and the thickness of the depletion layer, respectively. As an example of a typical silicon detector[9] we get d = 300 µm, U = 100 V and the transit time becomes[8] :

$$\tau_t = 6.7 \text{ ns} \quad \text{(for electrons)}$$
$$\tau_t = 22.1 \text{ ns} \quad \text{(for holes)}$$

The output current signal is proportional to the number of charged pairs divided by the transit time, see Para. 6.

7. COMPUTER SIMULATION

In order to cross check the evaluations presented in Para. 2, 3 and 4, a Monte-Carlo simulation has been carried out with a computer code which takes into account the exact synchrotron light production, the effects of a tungsten filter and the efficiency of a silicon detector.

The steps of the simulation run as follows :
First an electron is created in the vertical phase plane with a probability corresponding to a bi-Gaussian distribution as given by Equ. 5 and Equ. 6. This phase plane is located azimuthally at the centre of the SR source (field depth is not taken into account since its effect is negligible). Then a photon is simulated with energy ε and vertical angle ψ corresponding to the distribution of Equ. 17 (from Ref. 3) :

$$\frac{d^2P}{d_\psi d_\varepsilon} = 3ce_c/h\ i\gamma^2 r^2\ (1 + \gamma^2\psi^2)^2 \quad K^2_{\frac{2}{3}}(x) + \frac{\gamma^2\psi^2}{1 + \gamma^2\psi^2} K^2_{\frac{1}{3}}(x) \qquad (17)$$

where $r = \varepsilon/\varepsilon_c$ and $x = \frac{r}{2}(1 + \gamma^2\psi^2)^{3/2}$.

This photon is followed to its vertical position within the filtre. There it is renormalized to take into account the photoelectric absorption related to :

$$\sigma_{ph}\ [\text{b/atom}] = A\ Z^{4.5}\ \varepsilon^{-a}\ [\text{keV}] \qquad (18)$$

where the parameters A and a are obtained by fitting the data shown on Fig. 8 ($A = 0.32$, $a = 2.772$) for $\alpha < 70$ keV and $A = 1.15$, $a = 2.686$ for $\varepsilon > 70$ keV, (the K-shell discontinuity for tungsten).

At this point Compton and Rayleigh scattering cross-sections are computed for this photon according to Equ. 19 and Equ. 20.

We use the following empirical formula for the Compton scattering cross-section[10] :

$$\sigma_{com}\ [cm^2/atom] = \pi\gamma_e^2 \frac{C_1\xi + C_2\xi^2 + C_3\xi^3}{1 + d_1\xi + d_2\xi^2 + d_3\xi^3}\ , \qquad (19)$$

with $$\xi = \frac{1}{1 + g\ (\varepsilon/mc^2)}$$

where C_i, d_i and g have the following values :

$g = 0.22204$

C_1	= 1.6510	d_1	= 12.5013
C_2	= 9.3402	d_2	= -14.2004
C_3	= -8.3250	d_3	= 1.6991

Formula (19) describes the cross-section within an error of 0.1 % for photon energy of $0 \leq \varepsilon \leq 1$ MeV.

Rayleigh scattering is computed with a cross-section given by[9] :

$$\sigma_{Ry}\ [b/atom] = B\ \varepsilon^{-b}\ [MeV]\ . \qquad (20)$$

The parameters B and b are obtained by fitting the data in Fig. 8 and B = 0.836, b = 1.73 for the photon energies of 40 keV ≤ E ≤ 400 keV.

The non scattered part of the photon norm is summed at the detector and histogrammed for vertical position, renormalized for scattering and for detector efficiency, $\eta(\varepsilon)$.
The detector efficiency is described as :

$$\eta = D\ \varepsilon^{-d}\ [keV], \qquad (21)$$

where the parameters are D = 5069.0, d = 3.153[10].
The scattered part of the photon changes direction according to

$$\frac{d\sigma}{d\Omega} = C\ (1 + \cos^2\theta) \qquad (22)$$

which is an acceptable approximation for Compton scattering in the forward direction and is considered good enough for Rayleigh scattering since this latter effect plays a very small role numerically. During this process the photon energy, ε, is changed to ε'

$$\varepsilon' = \varepsilon \quad 1 + \frac{\varepsilon}{m\,c^2} (1 - \cos\,\theta) \qquad (23)$$

By following the new trajectory one obtains the vertical position at the detector for the scattered part of the photon which has to be normalized with detector efficiency $\eta(\varepsilon')$.

Finally the detected photon weight is converted into number of pairs created in the detector, when multiplied by $\varepsilon/\varepsilon_{pair}$, $(\varepsilon'/\varepsilon_{pair})$.

TABLE I

Summary of simulation steps

Electrons per bunch		$\frac{i}{4\ e\ f_{rev}}$	
Electron phase plane at source		$y_s,\ y'_s$	
Photon produced with		$\varepsilon,\ \psi$	
Photon phase space at filtre		$y_f,\ y'_f$	
Filtre absorption		$e^{-x/\lambda(\varepsilon)}$	
Photon scattering	$\theta = 0$		$0 < \lvert\theta\rvert < \pi/2$
New energy	ε		ε'
Position at detector	y_d		$\tilde{y}_d$
Detector efficiency	$\eta(\varepsilon)$		$\eta(\varepsilon')$
Pair creation	$\varepsilon/\varepsilon_{pair}$		$\varepsilon'/\varepsilon_{pair}$

where f_{rev} = revolution frequency 11.2 kHz

λ_{ph} = photoelectric absorption length

x = filtre thickness

ε_{pair} = energy for pair creation.

Figure 11 shows the number of simulated charged pairs in the detector as a function of photon energy. The effect of the K-shell edge in photoelectric cross-section is not seen because of the larger number of charged pairs created at higher incident photon energy according to Formula (23). The scattered photons traversing the filter are degraded in energy and can hardly be seen in the low energy tail of the spectrum.

In our simulation, the electron beam, if it could be measured when passing by detector position, would have the following width and divergence :

$$\sigma_y = 467.2\ \mu m$$
$$\sigma_{y'} = 11.97\ \mu rad\ .$$

The influence of the angular distribution of SR is demonstrated in Fig. 12 and 13. It enlarges the width up to :

$$\sigma_y = 485.8\ \mu rad,\quad \text{(see Fig. 13)},$$

and increases the divergence to :

$$\sigma_{y'} = 13.05\ \mu rad,\quad \text{(see Fig. 12)}.$$

With a tungsten filter of 4 mm thickness these values come back to :

$$\sigma_y = 480.5\ \mu m$$
$$\sigma_{y'} = 12.38\ \mu rad,$$

so that the measurable X-ray profile is only 2.8 % larger than the electron beam profile.

Figure 14 shows the performance of the filter. A thicker filter reduces more the effect of the angular distribution of SR, but yields more scattering and less signal. An optimum accuracy for the beam size is reached with, say, 4 mm thickness.

8. BUNCH OBSERVATION

For some investigations of beam dynamics it would be interesting to measure profiles integrated over a single bunch passage. Since the time interval between two successive LEP bunches is 22.5 μs, it will be easy to separate electronically the signals of the four bunches with a system such as analogue/digital converter, amplifier and multiplexer etc., but we must check that we got enough sensitivity. Figure 15 shows the profile signal generated by a single passage of a bunch (4 mm W filter in use). At the centre of the profile distribution we get 9150 induced charged pairs per strip of 60 μm and those pairs diffuse into the pand n-layers in the detector within 6.7 ns (Section 6). Thus the peak current is 219 nA. A limitation of the detectable signal is set by the thermal noise of the circuit.

$$\bar{i}_s^2 = \frac{4kTB}{R} \quad , \tag{24}$$

where
- k = Boltzman's constant
- T = absolute temperature
- B = band width
- R = resistance of the silicon slab.

This signal contains frequencies up to 166 MHz, however, the band width is limited by the circuit, say, to about 30 MHz. As an example we put T = 300 K, B = 30 MHz and R = 1 GOhm, and we get :

$$\bar{i}_s = 71 \text{ nA}$$

with a binning of 60 μm we get a signal of 219 nA at the center of the profile distribution (Fig. 15) and 133 nA at one standard deviation. The latter one is still detectable, however, we have to take great care in designing the system. In case of serious difficulties one could raise the signal by one order of magnitude just by reducing the filter thickness.

CONCLUSIONS

We investigated the feasibility of a beam profile measurement by direct detection of synchrotron light. The blow-up due to the angular distribution of the synchrotron light emission has been minimized by placing a filter in front of the detector. According to our computer simulation the photon beam profile at the detector plane will be only 2.8 % larger than would the electron beam profile be at the same place. A silicon microstrip detector should be suitable to measure profiles of individual bunches with plentyful spacial resolution and enough sensitivity in one passage. No fancy imaging system is required.

ACKNOWLEDGEMENTS

The authors are indebed to G. von Holtey for his contribution to understanding the effects of the filter and to E. Rossa for many discussions concerning silicon detectors.

REFERENCES

1. A.P. Sabersky,
Optical Beam Diagnostics on PEP,
IEEE Trans. NS-28 (1981) 2162;

R. Bossart, J. Bosser, L. Burnod, E. d'Amico, G. Ferioli, J. Mann and F. Méot,
Proton Beam Profile Measurements with Synchrotron Light,
CERN/SPS/80-8 (ABM);
see also Ref. 11 for general description of solid state detector.

2. J. Bosser, R. Caisson, A. Hofmann and F. Méot,
Possible Use of Synchrotron Radiation for Electron Beam Profile Monitoring in LEP and SPS,
LEP Note 397.

3. R.A. Mack,
Spectral and Angular Distribution of Synchrotron Radiation,
CEAL-1027 (1966).

4. C. Bovet,
Rayonnement synchrotronique, première partie, figure 5,
Lecture given in LEP-BI Group.

5. E.D. Courant and H.S. Snyder,
Theory of the alternating-gradient Synchrotron,
Ann. of Phys. 3 (1958) 1.

6. J.R. Hubbell,
Photon cross-sections, attenuation coefficients and energy absorption coefficients from 10 keV to 100 GeV,
NSRDS-NBS 29.

7. G. von Holtey,
Penetration of (LEP) Particles in Matter,
Lecture given in LEP-BI Group.

8. J.S. Worgan,
Energy dispersive Detectors for Synchrotron radiation,
Nucl. Instr. and Meth. 201 (1982) 85.

9. C. Hastings,
Jr. Approximations for Digital Computers,
Princeton University Press 1955,
and also see Ref. 6.

10. Catalogue of "Passivated Ion implanted Silicon Junction Detectors",
Schlumberger.

11. N.M. Allinson,
Solid-state imaging Arrays for X-ray Detection,
Nucl. Instr. and Meth. 201 (1982) 53.

P. Bonamy, P. Borgeaud and J. Mouchet,
Performance of Surface Barrier and Ion-implantation Silicon Detector,
EP Internal Report 81-06, CERN.

E.H.M. Heigne,
Muon Flux Measurement with Silicon Detectors in the CERN Neutrino Beams,
CERN 83-06.

FIGURE CAPTIONS

Fig. 1 Layout of the system

Fig. 2 Synchrotron light yield from a normal dipole in LEP phase I

Fig. 3 Angular distribution of synchrotron light

Fig. 4 Virtual phase plane transformation

Fig. 5 Phase plane ellipses (at 1 σ) for electron beam and hard X-ray photons

Fig. 6 Schematic illustration of field depth

Fig. 7 Ratio of photoelectric absoprtion to total scattering of photons for different materials

Fig. 8 Absorption and scattering of photons in tungsten, versus photon energy

Fig. 9 Tungsten filter attenuation, versus photon energy

Fig. 10 Silicon detector efficiency and filter attenuation factor, versus photon energy

Fig. 11 Energy spectrum of detected photons and corresponding number of charged pairs created in the detector

Fig. 12 Simulated beam divergence at detector position

Fig. 13 Simulated beam profile at detector position

Fig. 14 Simulated beam profile width versus filter thickness

Fig. 15 Histogram of a profile measured with 60 μm strips (results of a Monte Carlo simulation)

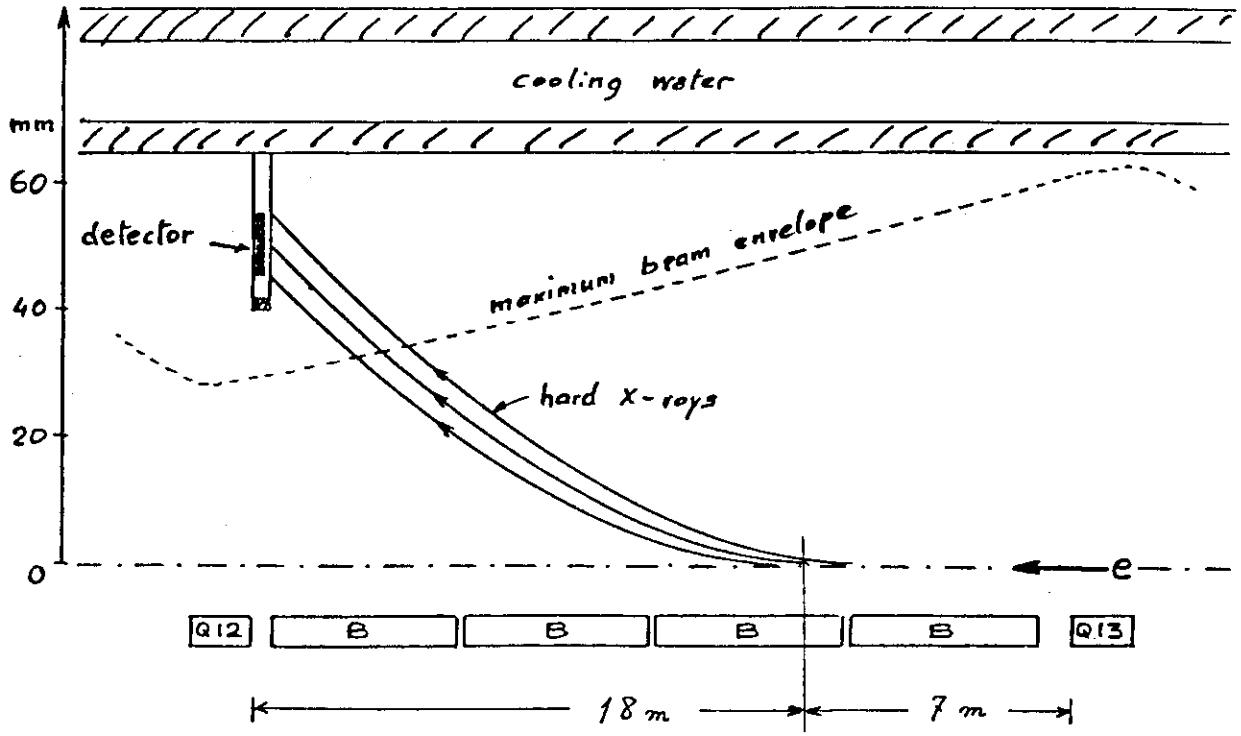
cooling water
mm
60
40
20
0
detector
maximum beam envelope
hard X-rays
e
Q12
B
B
B
B
Q13
18 m
7 m

Fig. 1

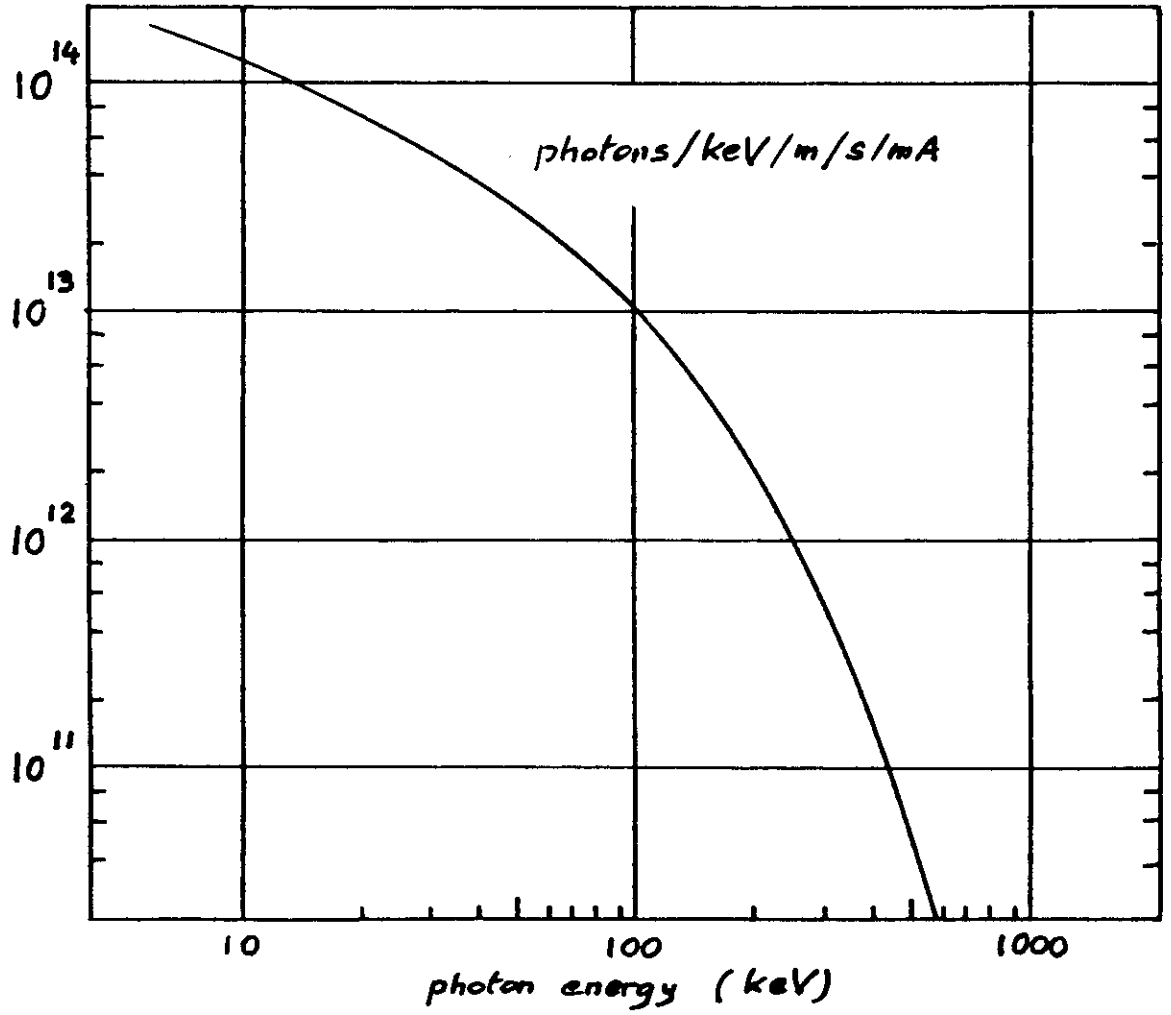
10^{14}
10^{13}
10^{12}
10^{11}
photons/keV/m/s/mA
10
100
1000
photon energy (keV)

Fig. 2

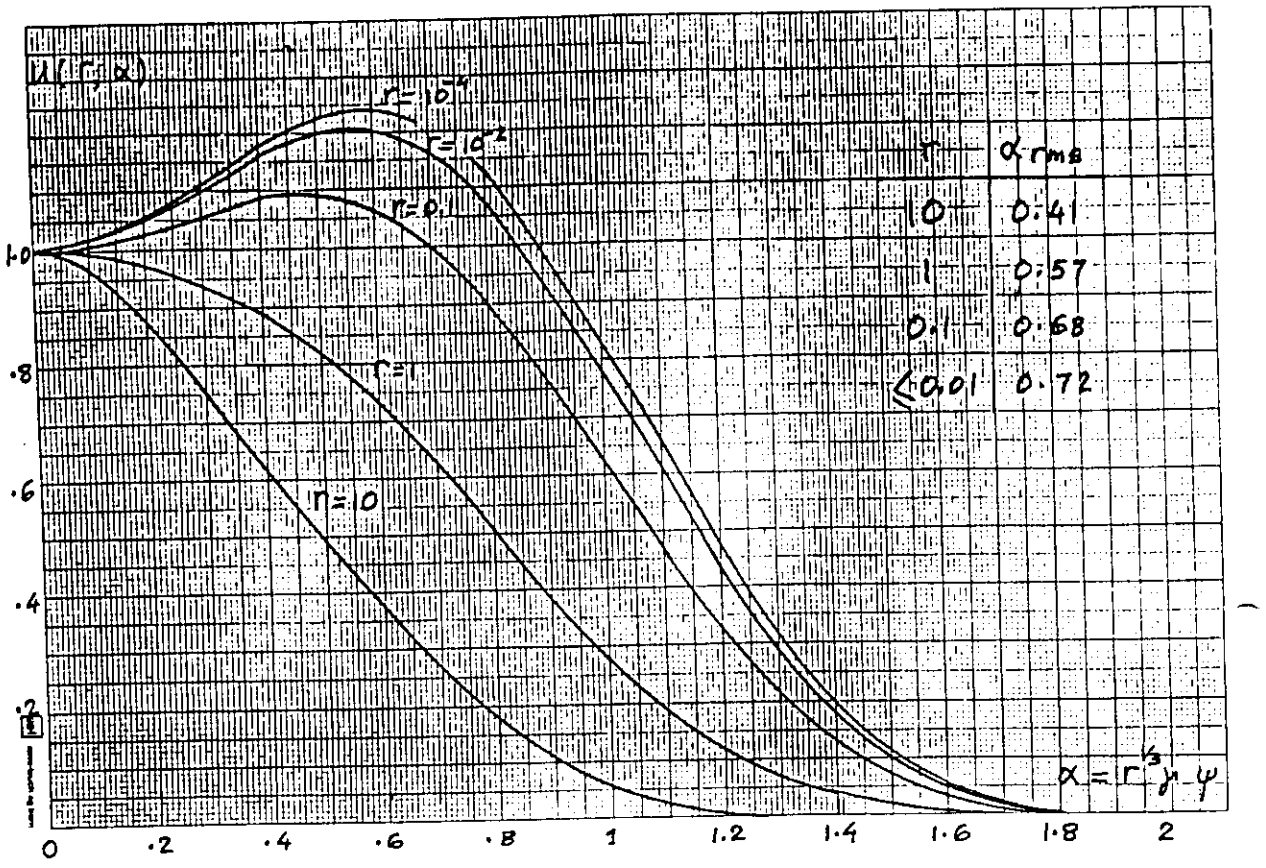

Fig. 3

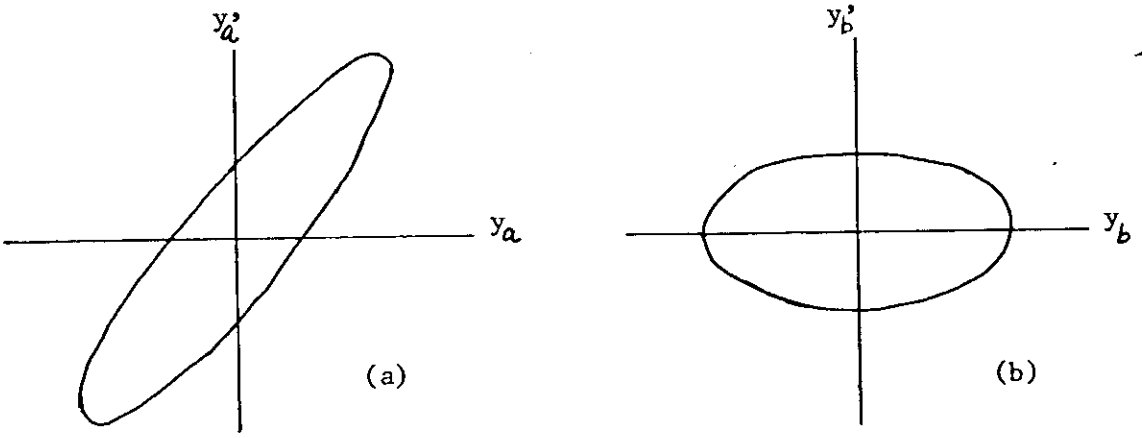

Fig. 4

Transformation of ellipse

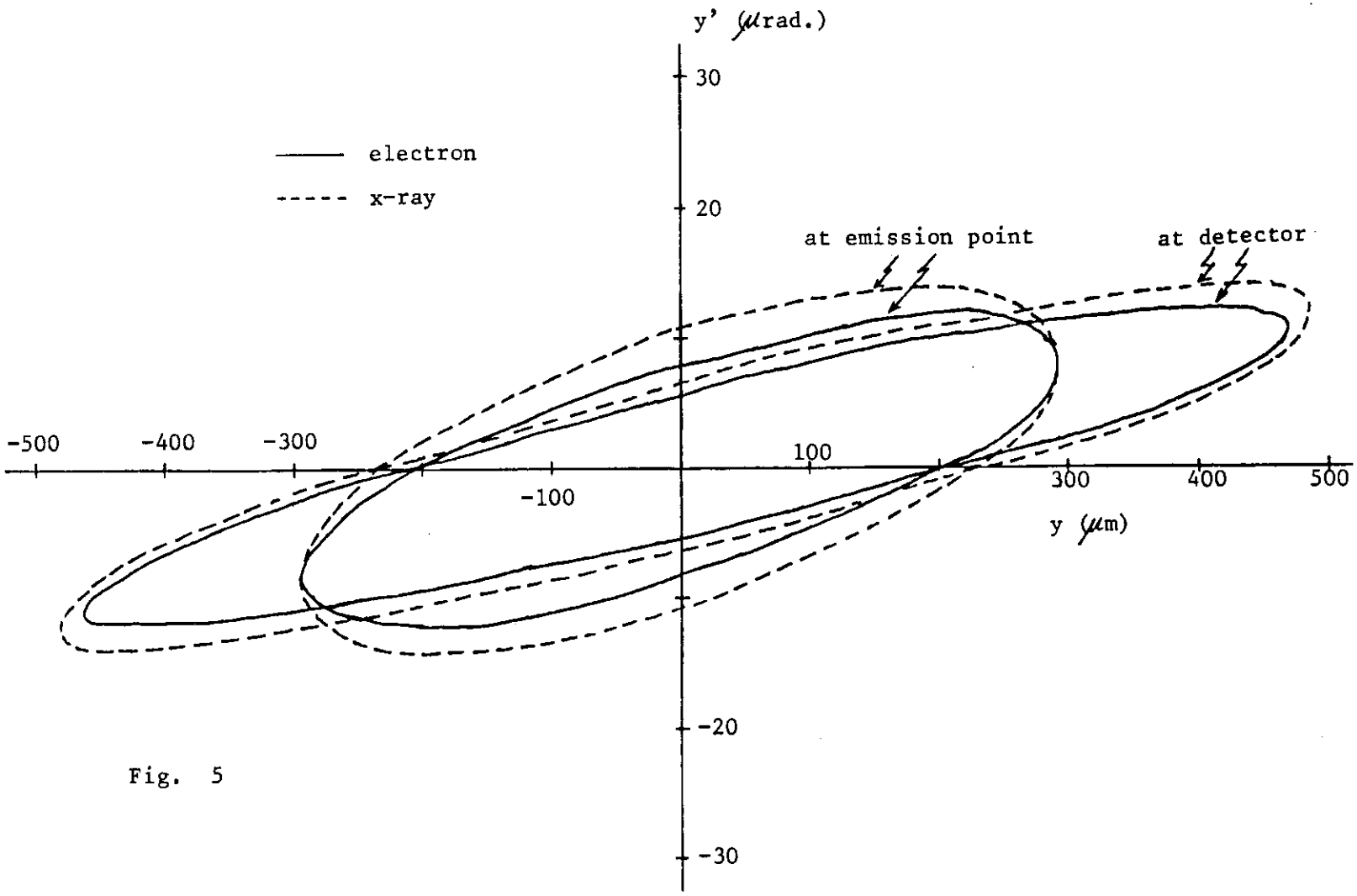
y' (μrad.)
30
20
-20
-30
electron
x-ray
at emission point
at detector
-500
-400
-300
-100
100
300
400
500
y (μm)

Fig. 5

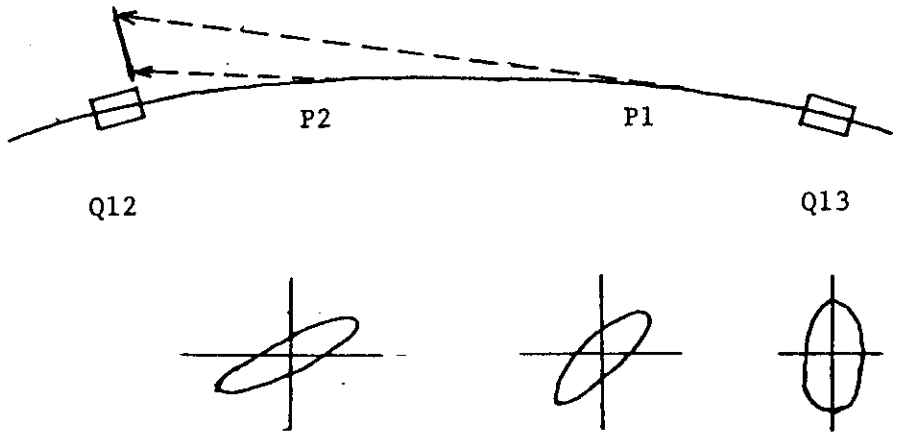

Fig. 6

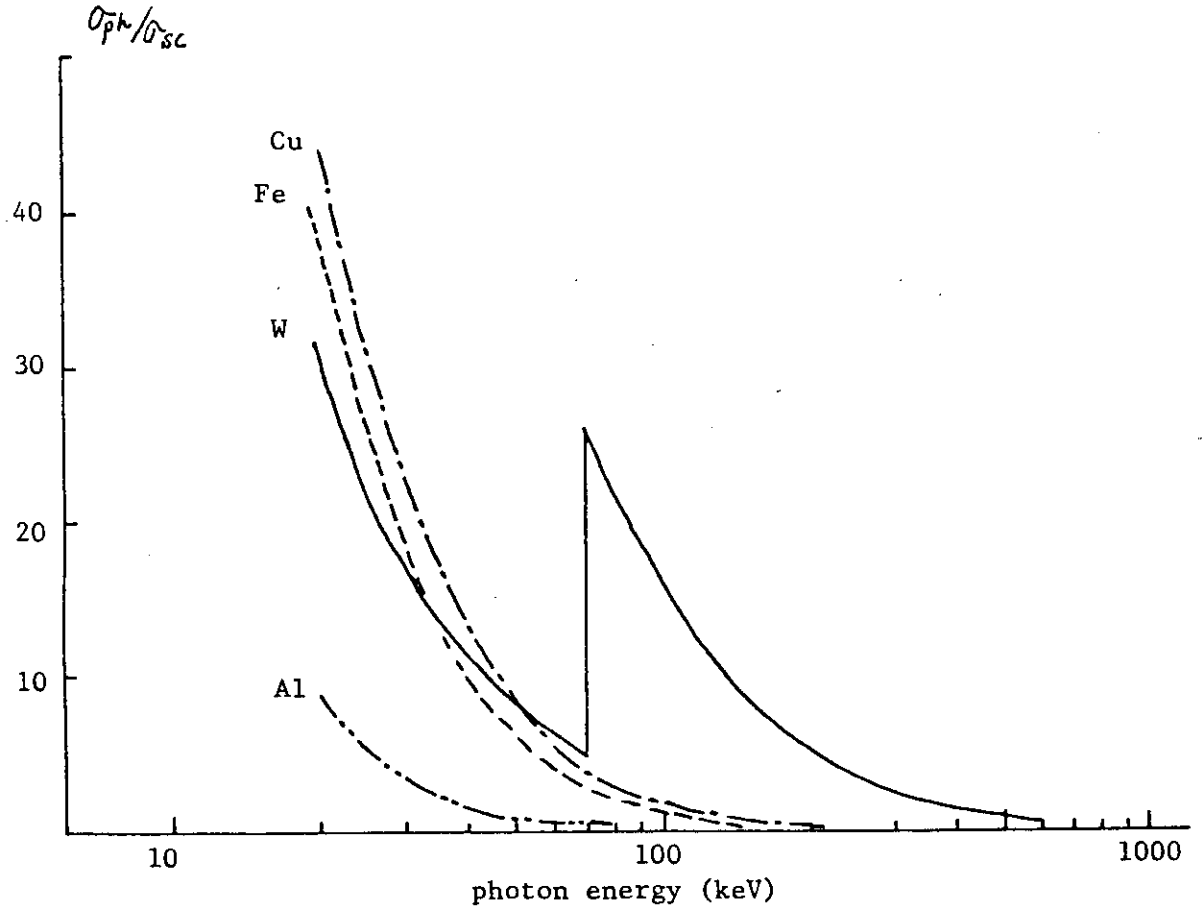

Fig. 7

Cross section ratio

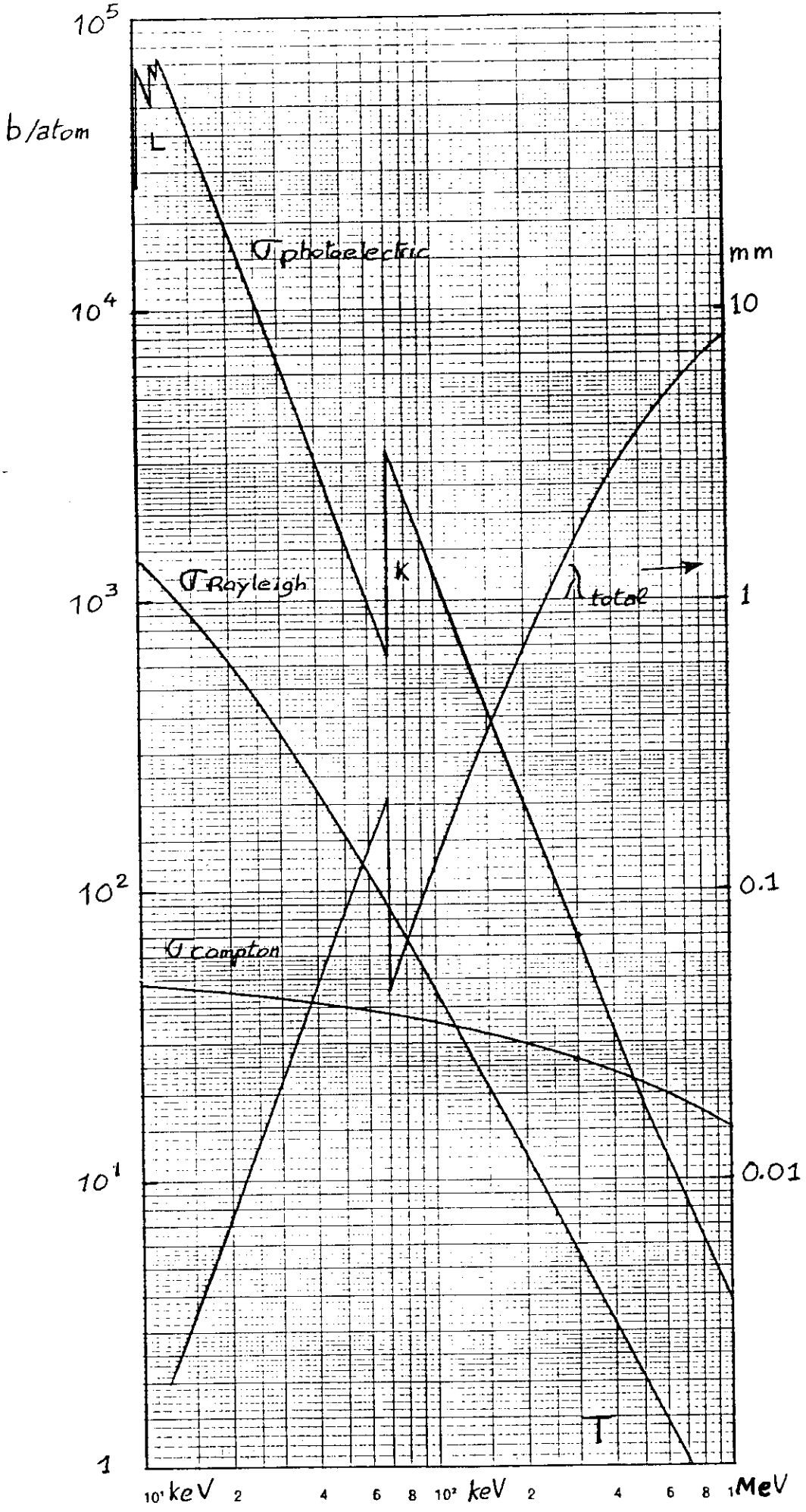
10^5
b/atom
L
$\sigma_{photoelectric}$
mm
10^4
10
K
$\sigma_{Rayleigh}$
λ_{total}
10^3
1
10^2
0.1
$\sigma_{compton}$
10^1
0.01
T
1
10^1 keV 2 4 6 8 10^2 keV 2 4 6 8 1 MeV

Fig. 8

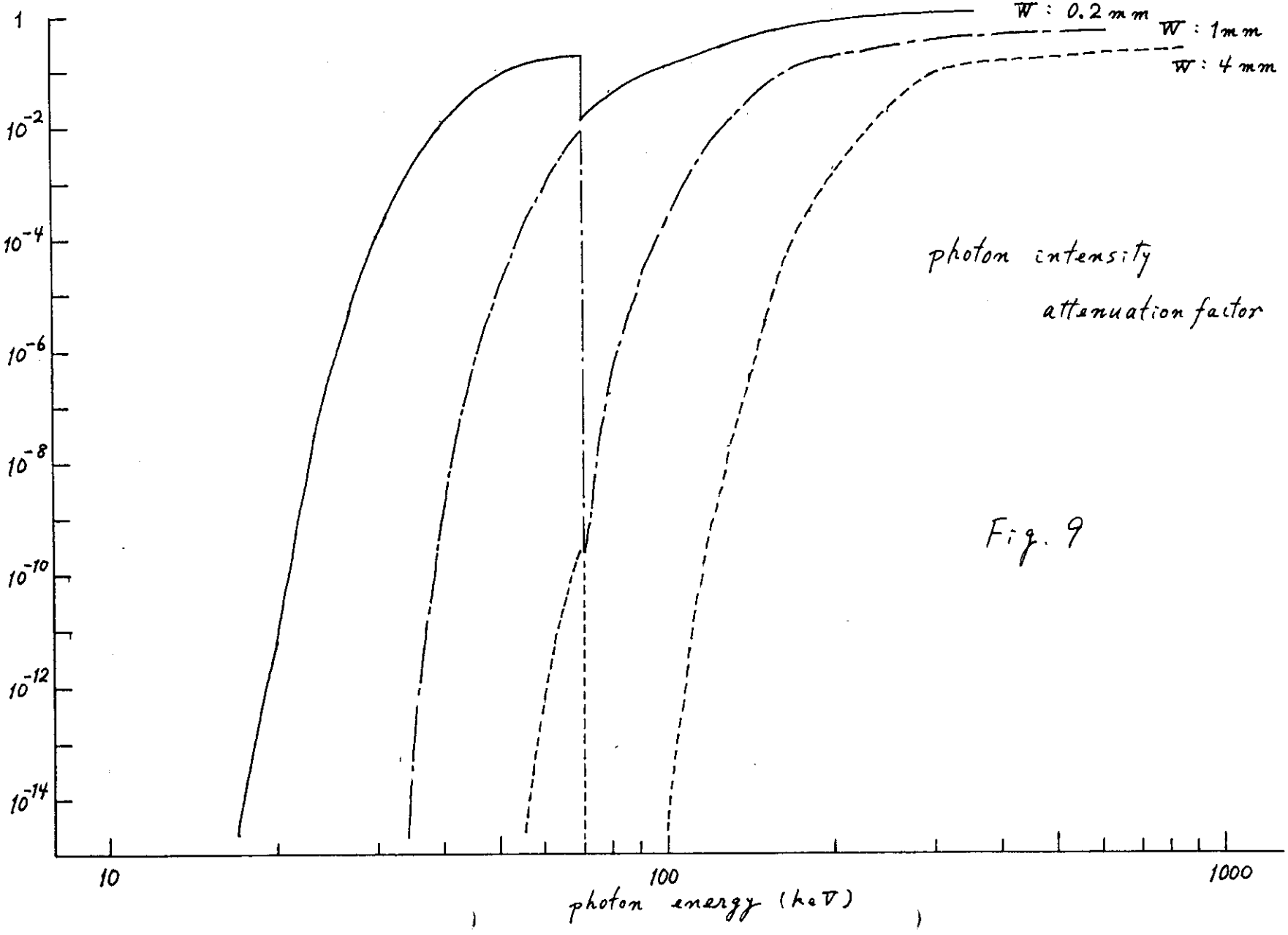
W : 0.2 mm
W : 1mm
W : 4 mm
1
10^{-2}
10^{-4}
10^{-6}
10^{-8}
10^{-10}
10^{-12}
10^{-14}
10
100
1000
photon energy (keV)
photon intensity
attenuation factor

Fig. 9

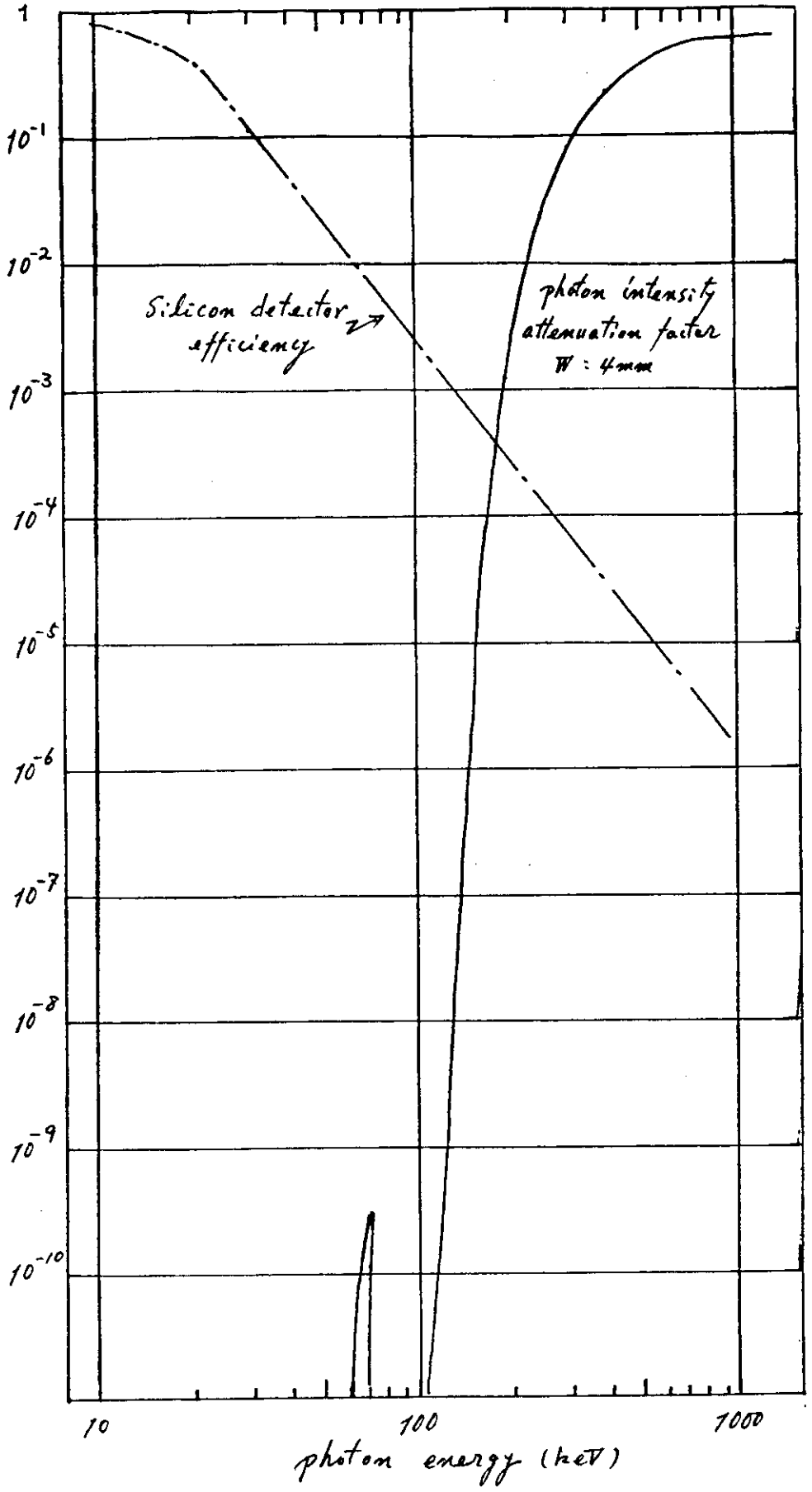
1
10^{-1}
10^{-2}
10^{-3}
10^{-4}
10^{-5}
10^{-6}
10^{-7}
10^{-8}
10^{-9}
10^{-10}
Silicon detector efficiency
photon intensity attenuation factor
W : 4mm
10
100
1000
photon energy (keV)

Fig. 10

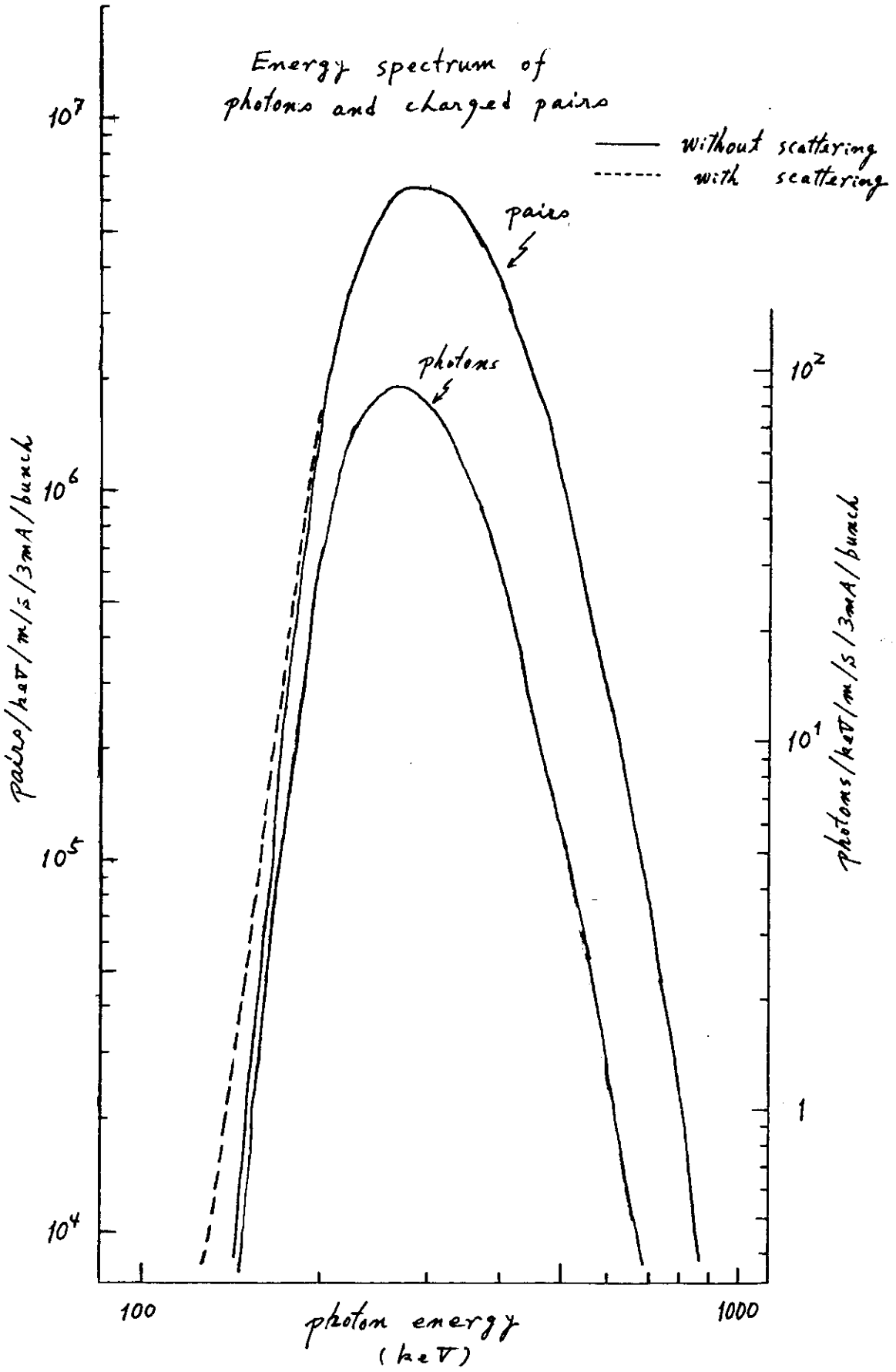
Energy spectrum of
photons and charged pairs
without scattering
with scattering
pairs
photons
10^7
10^6
10^5
10^4
10^2
10^1
1
pairs/keV/m/s/3mA/bunch
photons/keV/m/s/3mA/bunch
100
1000
photon energy
(keV)

Fig. 11

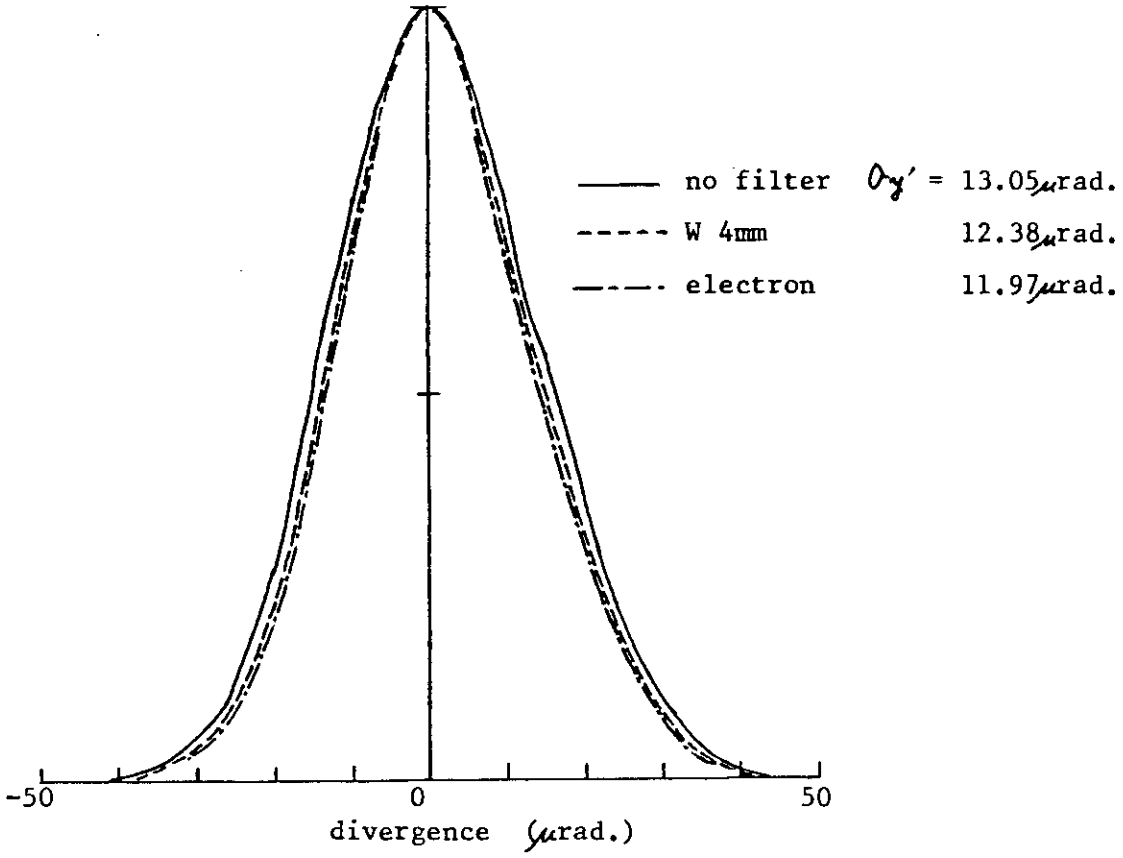
no filter $\sigma_{y'}$ = 13.05μrad.
W 4mm 12.38μrad.
electron 11.97μrad.
-50
0
50
divergence (μrad.)

Fig. 12

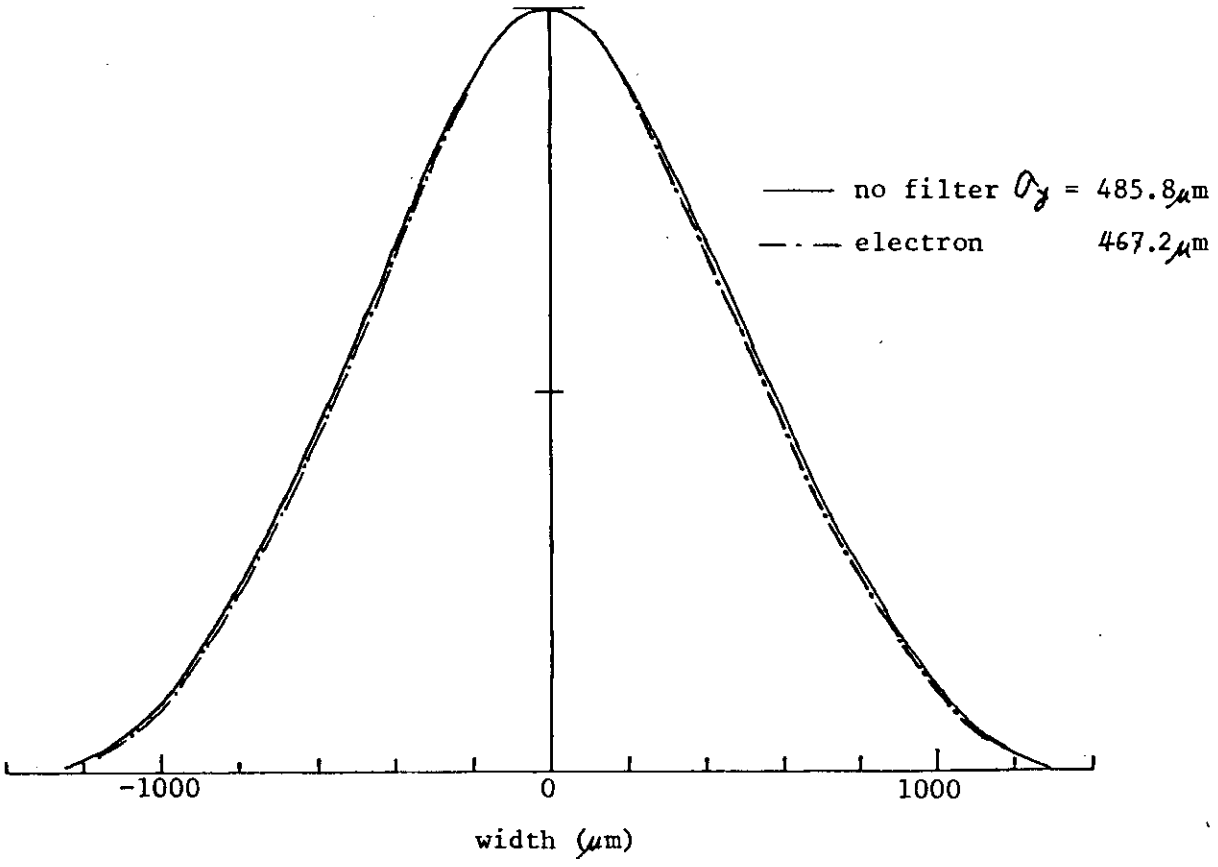
no filter σ_y = 485.8μm
electron 467.2μm
-1000
0
1000
width (μm)

Fig. 13

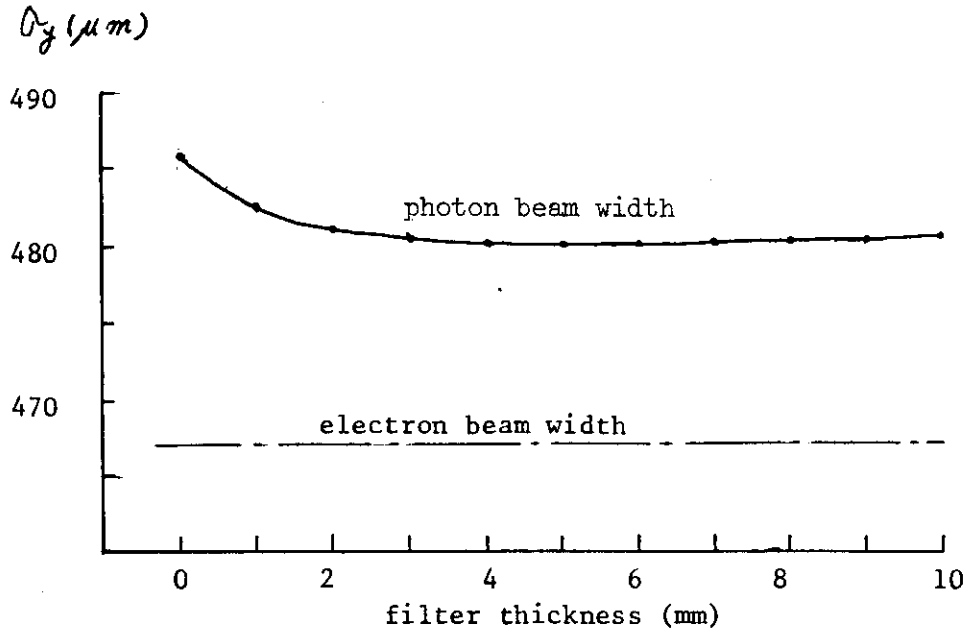
σ_y (μm)
490
480
470
photon beam width
electron beam width
0
2
4
6
8
10
filter thickness (mm)

Fig. 14

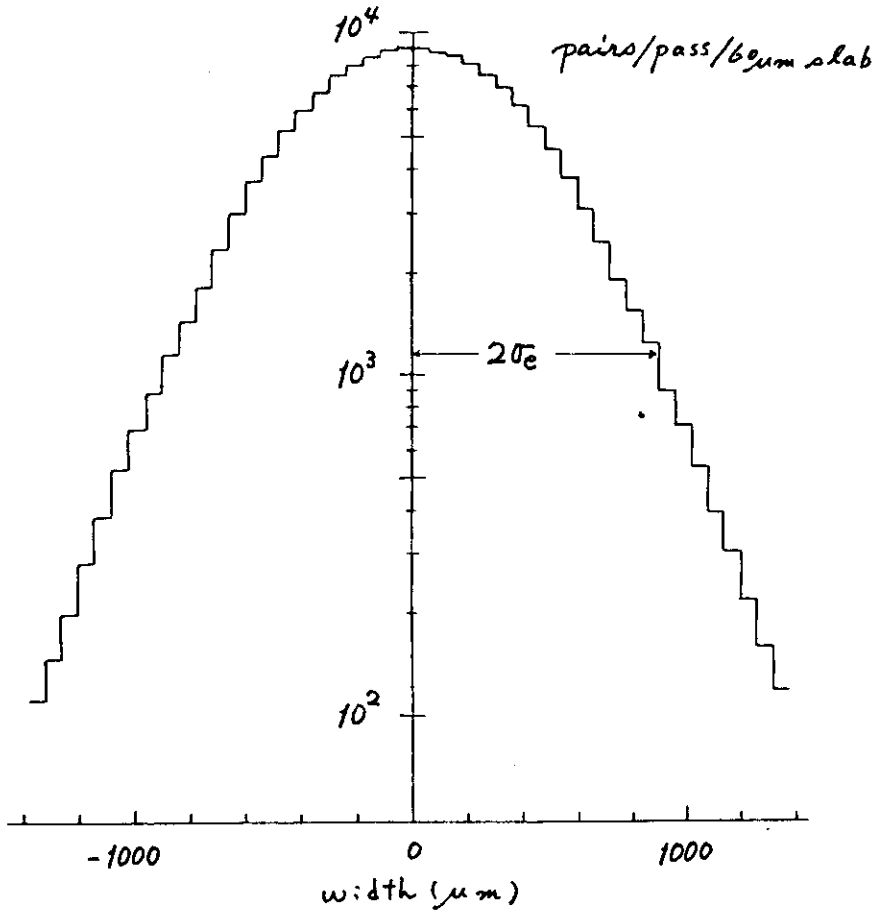
10^4
pairs/pass/60μm slab
10^3
$2\sigma_e$
10^2
-1000
0
1000
width (μm)

Fig. 15